

Article

Nanochannelar Topography Positively Modulates Osteoblast Differentiation and Inhibits Osteoclastogenesis

Raluca Ion ¹, Anca Mazare ², Cristina Dumitriu ³, Cristian Pirvu ³, Patrick Schmuki ² and Anisoara Cimpean ^{1,*} 

¹ Department of Biochemistry and Molecular Biology, University of Bucharest, 91-95 Splial Independentei, 050095 Bucharest, Romania; rciubar@yahoo.com

² Department of Materials Science, University of Erlangen-Nuremberg, WW-4, LKO, Matersstr 7, 91058 Erlangen, Germany; anca.mazare@fau.de (A.M.); schmuki@ww.uni-erlangen.de (P.S.)

³ Faculty of Applied Chemistry and Materials Science, University Politehnica of Bucharest, Str. Gheorghe Polizu 1-7, 011061 Bucharest, Romania; dumitriu.cristina.o@gmail.com (C.D.); cristian.pirvu@upb.ro (C.P.)

* Correspondence: anisoara.cimpean@bio.unibuc.ro; Tel.: +40-21-318-15-75 (ext. 106)

Received: 18 July 2018; Accepted: 20 August 2018; Published: 21 August 2018



Abstract: Based on previously reported findings showing reduced foreign body reactions on nanochannelar topography formed on TiZr alloy, this study explores the in vitro effects of such a nanostructured surface on cells relevant for implant osseointegration, namely osteoblasts and osteoclasts. We show that such nanochannelar surfaces sustain adhesion and proliferation of mouse pre-osteoblast MC3T3-E1 cells and enhance their osteogenic differentiation. Moreover, this specific nanotopography inhibits nuclear factor kappa-B ligand (RANKL)-mediated osteoclastogenesis. The nanochannels' dual mode of action on the bone-derived cells could contribute to an enhanced bone formation around the bone implants. Therefore, these results warrant further investigation for nanochannels' use as surface coatings of medical implant materials.

Keywords: topography; nanochannels; osteoblast; macrophage; osteoclast

1. Introduction

Among various surface modification techniques, electrochemical anodization has been intensively explored to synthesize biologically-inspired nanostructures on titanium (Ti) and its alloys [1]. Experimental studies provide evidence that, for example, nanotubes that mimic bone patterning are superior in promoting early biological events related to the adsorption of proteins [2] and osteoblastic differentiation both in vitro and in vivo [3–8]. Moreover, it was demonstrated that nanotube-modified Ti surfaces elicit an attenuated inflammatory macrophage response [9–12] and an increased anti-bacterial activity [8,13] when compared to flat Ti substrates.

The properties of nanostructures produced by electrochemical anodization depend on the anodization conditions used, such as electrolyte [14], pressure [15], anodizing voltage, and temperature. For example, different morphologies have been produced, including bamboo tubes and branched tubes by changes in the applied anodization voltage, or spaced nanotubes in specific electrolytes (diethylene glycol, tri-ethylene glycol, dimethyl sulfoxide, etc.) at room temperature and ambient pressure [14], while longer nanotubes were fabricated under negative pressure as compared to atmospheric conditions [15]. Usually, when anodization is performed in organic electrolytes containing NH₄F (i.e., glycerol or ethylene glycol electrolyte) with low amounts of water, TiO₂ nanopore or nanotube arrays can be fabricated [2,16,17], and the water content and the applied voltage determine the morphology type (contributes to the formation of nanotubes from nanopores by

a pore-wall splitting mechanism). The nanostructures' characteristics (inner or outer pore/tube diameter, length) are dependent on the anodizing potential, time, and electrolyte temperature. On the other hand, micrometer thicknesses can be grown without observing a drop in the growth rate with time. In our previous study [18], we reported a simple, inexpensive method for the generation of mesoporous structures, i.e., aligned oxide nanochannels, on Ti50Zr alloy, by anodization in hot glycerol-phosphate electrolytes. Initial cell characterization revealed a reduced number of metabolically-active macrophages on nanochannels, a low potential to induce macrophage fusion into foreign body giant cells, and a low concentration of pro-inflammatory cytokines in the culture medium. Thus, the incorporation of nanochannel architecture on the surface of biomaterials has been shown to provide a unique means to limit foreign body response-associated cell–cell fusion, which could lead to improved biomaterial-tissue integration and performance. In the present study, an *in vitro* investigation of osteoblast cell-surface interaction on these nanomorphologies was conducted. Thus, cell viability, proliferation and differentiation studies were performed, which offer clues to the nature of osteoblast cell response elicited by the nanochannels. In addition to osteoblast differentiation, the effect of nanochannel substrates on osteoclastogenesis was also evaluated by quantification of tartrate-resistant acid phosphatase (TRAP) protein expression and activity and actin cytoskeleton staining of the receptor activator of nuclear factor kappa-B ligand (RANKL)-stimulated RAW 264.7 cells.

2. Materials and Methods

2.1. Samples Preparation and Characterization

Nanochannels were formed on TiZr alloy pieces (2 cm × 2 cm) containing 50 wt % Ti and 50 wt % Zr (from ATI Wah Chang Co., Albany, OR, USA) as previously described [18]. Briefly, prior to anodization, TiZr pieces were chemically etched in a cold acid mixture (HNO₃:HF:H₂O in a 3:1:2 ratio) for 10 s, rinsed with deionized water (DI) and dried in a N₂ stream. The electrolyte composed of 10 wt % K₂HPO₄/glycerol was first continuously stirred at 200 °C for 4 h (to remove all traces of water), followed by decreasing the temperature to 180 °C and starting the anodization of the freshly conditioned TiZr sample in a two-electrode setup (Pt–cathode, TiZr–anode) for 2 h at 50 V (Voltcraft VSP 2653 electrochemical source). Polished TiZr samples were used as control samples. The morphology of the nanostructure was evaluated by scanning electron microscopy (Hitachi field emission scanning electron microscope (FE-SEM) S4800, Tokyo, Japan). Water contact angle (CA) measurements were performed to evaluate sample's wettability (Angle Meter–CAM 100, KSV Instruments Ltd., Helsinki, Finland). Additionally, the topography and roughness were investigated by atomic force microscopy (AFM) from a 50 × 50 μm² scan area, contact-mode AFM images–APE Research, Trieste, Italy (Gwyddion software, version 2.50).

2.2. Cell Culture Model

Mouse pre-osteoblast MC3T3-E1 cells (Subclone 4, ATCC[®], CRL-2593[™], Manassas, VA, USA) were used in the current study. The cells were maintained in Dulbecco's minimal essential medium (DMEM, Sigma-Aldrich Co., St. Louis, MO, USA) supplemented with 10 vol % foetal bovine serum (Gibco, Life Technologies Corporation, Grand Island, NY, USA) and 1 vol % penicillin/streptomycin (10,000 units/mL penicillin and 10 mg/mL streptomycin) (Sigma-Aldrich Co. St. Louis, MO, USA) under standard culture conditions (37 °C, 5% CO₂). The culture media were refreshed every 48 h.

2.3. Cell Morphology

Morphologies of MC3T3-E1 cells cultured on flat and nanostructured surfaces were observed by SEM and fluorescence microscopy. Briefly, the cells were seeded onto substrates at a density of 10,000 cells/cm². At 2 and 24 h after seeding, the cells were processed for SEM, as previously described [19].

To prepare samples for fluorescence microscopy observation, the cells were fixed with 4% paraformaldehyde (in phosphate buffered saline (PBS)) for 20 min, permeabilized by incubation with 0.1% Triton X-100/2% bovine serum albumin (BSA) for 15 min at room temperature and stained with Alexa Fluor 488 Phalloidin (20 µg/mL, Invitrogen, Eugene, OR, USA) for 15 min to label cytoskeletal filamentous actin (F-actin) and counterstained with 4'-6-diamidino-2-phenylindole (DAPI) (Sigma-Aldrich Co., Steinheim, Germany) for 15 min to label the cell nuclei. Thereafter, representative images observed with an inverted fluorescence microscope (Olympus IX71, Olympus, Tokyo, Japan) were captured using Cell F software (Version 5.0).

2.4. Cell Viability and Proliferation

MC3T3-E1 cells were seeded onto tested surfaces at a density of 10,000 cells/cm². Cell viability was evaluated using a Live/Dead Viability/Cytotoxicity Kit (L-3224, Molecular Probes, Eugene, OR, USA). At day 1 and 4 after seeding, the cells were washed with PBS and stained for 15 min at 37 °C with 2 mM calcein-AM to label the live cells (green fluorescence) and 4 µM ethidium homodimer to label the dead cells (red fluorescence). Thereafter, the samples were imaged under a fluorescence microscope (Olympus IX71, Olympus, Tokyo, Japan).

Cell proliferation was monitored at the same time points following cell incubation for 3 h at 37 °C with 1 mg/mL MTT (3-(4,5-Dimethyl-2-thiazolyl)-2,5-diphenyl-2H-tetrazolium bromide) solution in serum-free culture medium, as we previously reported [20].

2.5. MC3T3-E1 Cell Differentiation

MC3T3-E1 cells were seeded onto the analyzed surfaces at a density of 40,000 cells/cm². After 2 days of culture, osteogenic differentiation was induced by incubating the cell-populated substrates in growth medium supplemented with 50 µg/mL ascorbic acid (Sigma-Aldrich Co., Steinheim, Germany) and 5 mM beta-glycerophosphate (Sigma-Aldrich Co., Steinheim, Germany). The media were refreshed every 48 h. Osteogenic differentiation of MC3T3-E1 cells was investigated by analyzing alkaline phosphatase (ALP) activity in cell lysates, osteocalcin expression and extracellular matrix mineralization.

Intracellular ALP activity in the cell lysates was measured using Alkaline Phosphatase Activity Colorimetric Assay Kit (BV-K412-500, BioVision, Milpitas, CA, USA) on the 7th and 14th day of osteoinduction [21]. The ALP activity was normalized by the total protein content determined with the Bradford reagent, according to the manufacturer's guidelines.

Immunofluorescence staining was performed to detect the expression of osteocalcin. For this, pre-osteoblast cells grown on the above substrates were fixed, permeabilized, blocked and incubated with specific antibodies, as previously reported [22]. Samples were observed under fluorescence microscopy (Olympus IX71, Olympus, Tokyo, Japan) and the images analyzed using Fiji/ImageJ version 1.52b (NIH, Bethesda, MD, USA; <https://imagej.net/Fiji>).

Extracellular matrix mineralization was determined by staining with Alizarin red S (AR-S) on day 21 after osteogenic induction according to the method already described in a previous paper [23]. Briefly, the cell-populated samples were fixed with 10% paraformaldehyde for 30 min, and then stained with 0.1% AR-S in distilled water (pH 4.0) for 1 h at room temperature. The air-dried samples were incubated in 5 vol % perchloric acid to solubilize and release calcium-bound AR-S into the solution. The absorbance of the released AR-S was measured at 405 nm using a microplate reader (Thermo Scientific Appliskan, Vantaa, Finland).

2.6. Osteoclast Differentiation

RAW 264.7 cells were plated on to substrates at an initial seeding density of 10,000 cells/cm² and cultured in DMEM containing 10% FBS and 50 ng/mL mouse recombinant receptor activator of RANKL. Every 2 days, the culture medium was replaced until mature osteoclasts were formed.

To evaluate morphology, differentiation and multi-nuclearity, the cells were stained for actin and cell nuclei as described in Section 2.3. The cells containing at least three nuclei were identified as osteoclasts.

The expression of TRAP within cells grown on nanochannelar and polished surfaces was investigated by immunofluorescence staining. After 7 days' incubation period, the samples were washed 2 times with PBS and the cells were fixed with 4% paraformaldehyde for 20 min. Subsequently, permeabilization of cell membranes was achieved by treatment with 0.1% Triton X-100 followed by incubation with 2% BSA in PBS. The samples were then incubated with rabbit anti-mouse TRAP antibody (Santa Cruz Biotechnology, Dallas, TX, USA) in PBS containing 1.2% BSA followed by three washes with PBS. Finally, the cell populated substrates were labeled with Alexa Fluor 488-conjugated goat anti-rabbit IgG antibody (Invitrogen, Eugene, OR, USA) in PBS containing 1.2% BSA. Cell nuclei were stained with DAPI. Samples were imaged using a fluorescence inverted microscope (Olympus IX71, Olympus, Tokyo, Japan). Multinuclear TRAP-positive cells were counted in five random regions and data are expressed as the number of TRAP⁺/mm².

TRAP intracellular activity was also evaluated after 7 days of culture using 4-nitrophenyl phosphate disodium hexahydrate (pNPP disodium hexahydrate; (Sigma-Aldrich Co., Steinheim, Germany)) as a chromogenic substrate to examine the inhibitory effects of nanochannels on osteoclast differentiation. 50 µL of cell lysate were incubated with 150 µL of TRAP substrate (at pH 5.5–6.1) consisting of 7.6 mM p-NPP in 100 mM sodium acetate buffer containing 50 mM disodium-tartrate dihydrate (Sigma-Aldrich Co., Steinheim, Germany) for 1 h at 37 °C. The enzymatic reaction was stopped by adding 50 µL of 3 M NaOH. The activity of the enzyme was measured at 405 nm by using a microplate reader (Thermo Scientific Appliskan, Vantaa, Finland).

2.7. Statistical Analysis

All samples were analyzed in triplicate. Data are presented as mean value ± standard error of the mean (SEM) and examined statistically by Student's *t*-test. Values of *p* < 0.05 were considered statistically significant.

3. Results and Discussion

3.1. Materials Characterization

The morphological and chemical characterization of the nanochannelar surface used in the present work was previously described [18]. Briefly, the morphology of nanochannels consists of ~35 nm diameter and 3.2 ± 0.6 µm length (the top morphology is shown in Figure 1); note that the needle-like microstructure of the alloy is also transferred to the nanostructure. Such nanochannels present a partially crystalline structure and consist of TiO₂, ZrO₂ and some small amounts of zirconium titanate or other mixed oxides [18]. In addition, the nanochannelar surface exhibits a higher hydrophilicity than the flat surface, i.e., the nanochannelar samples have an average contact angle (CA) of $15^\circ \pm 0.7$ while the polished control has a less hydrophilic surface with a CA of $80^\circ \pm 3.8^\circ$.

The topography of the studied films was investigated using AFM in contact mode. As presented in Figure 2, AFM analysis showed distinct roughness for the flat and nanochannelar surfaces. Namely, the nanochannelar surface has a higher roughness with an R_{ms} (root mean square roughness) of 0.352 m, while R_{ms} for the flat substrate was 0.085 m.

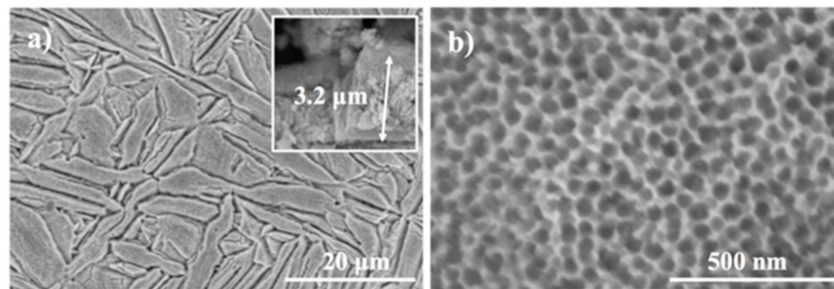


Figure 1. Morphology of nanochannels on TiZr substrates: (a) low magnification top view and cross-section in inset; (b) high magnification top view scanning electron microscope (SEM) images.

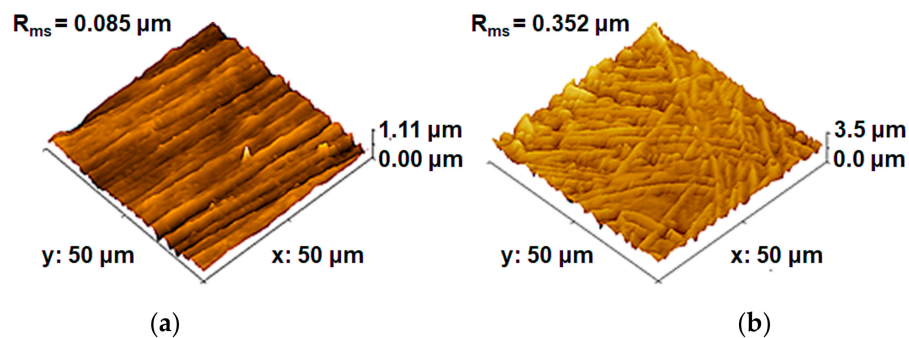


Figure 2. Atomic force microscopic (AFM) images of flat TiZr (a) and nanochannelar TiZr surfaces (b).

3.2. In Vitro Osteoblast Behavior

3.2.1. Cell Morphology

To characterize how pre-osteoblast cells interact with the nanochannelar surface, cells were cultured on such topographically modified surfaces including a smooth substrate as control. The morphological appearance of the adhered cells was evaluated by SEM (Figure 3) and actin fluorescent staining (Figure 4).

After 2 h of incubation, most cells exhibited a rounded form, which is typical for the first phases of substrate adhesion. Yet, a comparison between the cells grown on control samples and those grown on nanochannels indicates that, even after just 2 h, the latter ones anchor themselves to the surface through long dendritic filopodia, while on the flat substrate the cells exhibited many thin filopodia for attaching to the surface. Also, osteoblastic cells underwent relatively less cell spreading on the nanochannelar surfaces. After 24 h of culture, cell spreading was achieved and specific morphologies could be observed in SEM. Thus, well-spread cells displaying a polygonal morphology were observed on the control substrate, whereas they presented a slender and elongated shape on the nanochannels.

As cell spreading is controlled by cytoskeleton arrangement, phalloidin conjugated with Alexa Fluor 488 was used to stain actin filaments (Figure 4). Fluorescence microscopy analysis performed at 2 h post-seeding revealed different cytoskeleton organization on the analyzed surfaces. Thus, on the flat TiZr substrate, circumferential localization of actin filaments near the cell membrane and some parallel oriented actin filaments throughout the cell body were observed. On the contrary, actin cytoskeleton on nanochannels appeared less organized and more diffuse. At a later time point (24 h after cell seeding), the cells in contact with the control surface adopted a typical osteoblast morphology and showed a normal organization of actin filaments. On the other hand, on the nanochannels, the pre-osteoblast cells were rather elongated and the actin filaments were more densely distributed in the cell periphery.

All these morphological results show that the nanostructured layer obtained by anodization has an important effect on cell adhesion and spreading. A possible explanation for this behavior consists in the constraints on cell morphology imposed by the surface topography. Moreover, differences

in surface chemistry and surface wettability between the nanochannels and the polished substrates would be anticipated to support differences in the conformation of the proteins adsorbed on their surface, that may also be important in influencing osteoblast morphology and function.

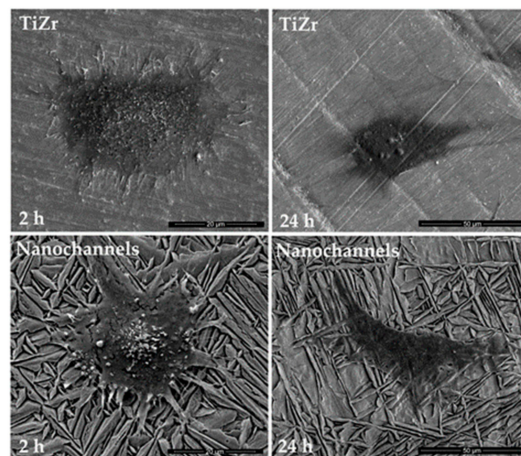


Figure 3. SEM images of MC3T3-E1 cells attached on the nanochannelar and flat TiZr surfaces imaged at 24 h post-seeding.

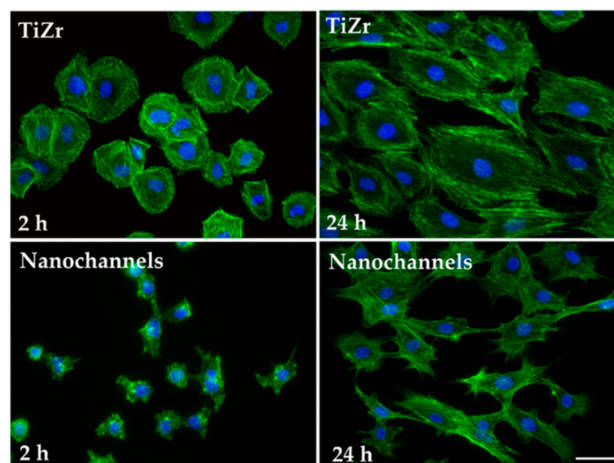


Figure 4. Fluorescence micrographs of MC3T3-E1 pre-osteoblasts in contact with the flat and nanochannelar TiZr samples for 24 h. The cells are labeled for F-actin (green) and nucleus (blue). Scale bar represents 50 μm .

3.2.2. Cell Viability and Proliferation

Live/Dead assay revealed a high percentage of living cells (green fluorescence) suggesting that the MC3T3-E1 cells survived and multiplied on both substrates analyzed (Figure 5a). Prolonged culture time led to an increased cell density, but the number of viable cells monitored using fluorescence imaging on nanochannels appeared to be lower than on the control substrate, especially at 4 days post-seeding. This finding was confirmed by MTT assay (Figure 5b), which showed that at 4 days post-seeding, the number of viable cells on the flat surface was 35% lower than on the nanochannelar substrate. We speculate that the lower optical density (OD) values exhibited by the MC3T3-E1 cells grown on nanochannels represent the beginning of the cell osteogenic differentiation. Therefore, we further assessed the osteoinductive potential of nanochannels under osteogenic culture conditions.

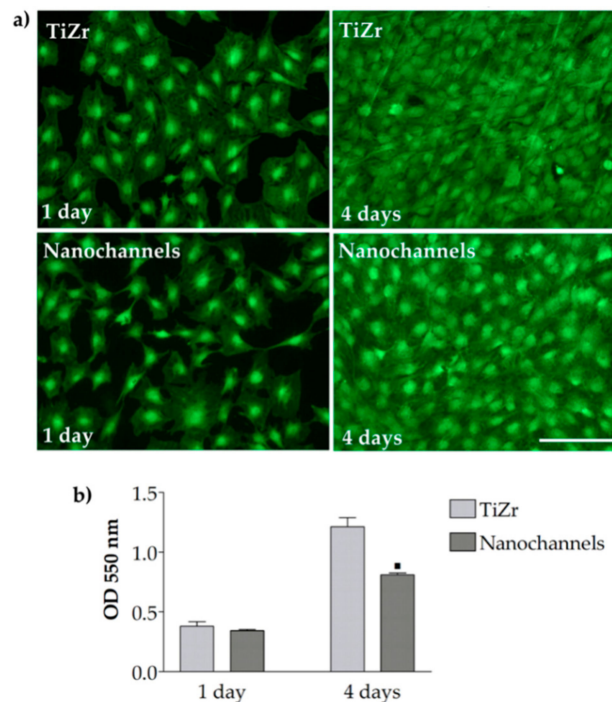


Figure 5. (a) Fluorescent images of the MC3T3-E1 cells grown for 1 and 4 days in contact with flat and nanochannelar substrates after staining with the Live/Dead Cell Viability/Cytotoxicity Assay Kit (live cells are green stained). Scale bar represents 200 μm ; (b) Proliferation of MC3T3-E1 pre-osteoblasts as assessed by MTT assay. Data analysis was based on mean \pm standard error of the mean (SEM) ($n = 3$); $p < 0.05$ vs. control.

3.2.3. Pre-Osteoblast Cell Differentiation

Osteoblastic differentiation is a multistep process involving a number of proteins being expressed at each stage [24]. In our study, osteoblast activity and differentiation were tested through the analysis of ALP activity, osteocalcin protein expression and extracellular matrix mineralization. ALP is regarded as a marker for early osteoblastic differentiation, whereas secretion of osteocalcin and matrix mineralization are associated with the final differentiation phase.

The ALP activity of MC3T3-E1 cells was measured after incubation for 1 and 2 weeks under osteogenic culture conditions. As shown in Figure 6a, ALP exhibited no differences among the experimental groups after 7 days, but significantly higher ALP activity was detected in pre-osteoblasts cultured on nanochannels than those grown in contact with flat TiZr for 2 weeks. Thus, ALP activity data suggest that the nanochannels augment osteogenic differentiation of the cells. The change in topography of the TiZr surface appeared to influence also osteoblast terminal differentiation, as assessed by osteocalcin expression. Specifically, after 21 days of culture the nanochannelar surfaces significantly increased osteocalcin expression when compared to the flat substrates (Figure 6b,c). The mineral deposition on the samples was evaluated by ARS staining, which was followed by elution and quantification at an absorbance of 405 nm. As can be seen in Figure 6d, nanochannels showed more mineralized extracellular matrix when compared to the flat TiZr surfaces.

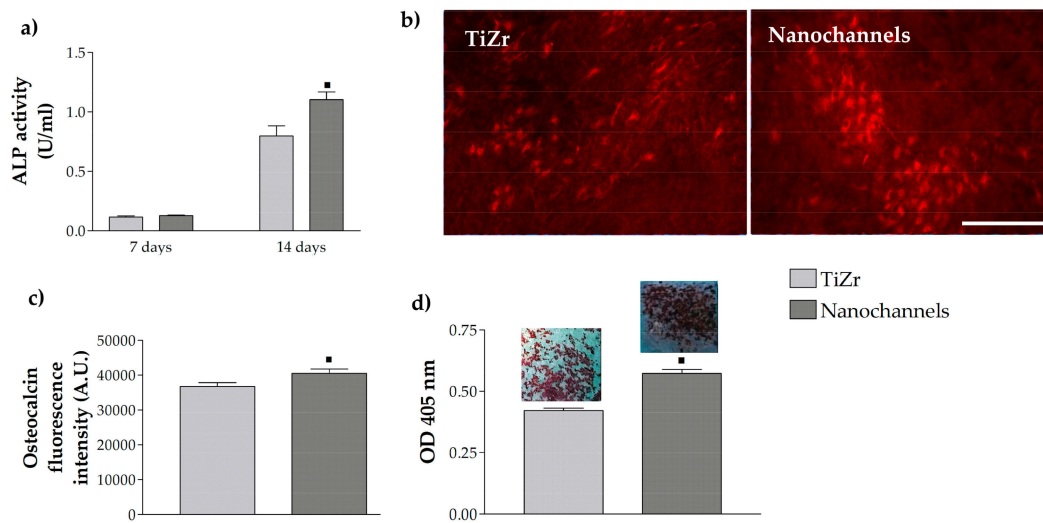


Figure 6. Differentiation of MC3T3-E1 pre-osteoblasts grown on the analyzed samples. (a) The expression levels of intracellular alkaline phosphatase (ALP) activity at 7 and 14 days post-seeding; (b) immunofluorescence detection of osteocalcin expression by MC3T3-E1 cells grown for 3 weeks on tested samples. Scale bar represents 200 μm . (c) Quantification of osteocalcin intensity using ImageJ; (d) quantitative colorimetric analysis of extracellular matrix mineralization after 3 weeks of culture and the staining pictures. Results are presented as means \pm SEM ($n = 3$); $p < 0.05$ vs. control.

Overall, the results indicated that all analyzed markers of the osteogenic differentiation were better expressed on nanochannels. The different degrees of cellular modulation by nanochannelar and flat substrates underline that surface topography has an important effect on osteogenic differentiation. Indeed, a large number of studies using different cell types have shown that cellular features such as adhesion, morphology, as well as cytoskeleton organization and osteogenic differentiation, are highly affected by surface topography [25–32]. Thus, nano- or micro-rough Ti surfaces were found to reduce osteoblast cells' proliferation and to enhance differentiation and local factor production, supporting a mature secretory osteoblast-like phenotype [33–36]. Moreover, elongation and stretching of osteogenic progenitors as a result of their interaction with topographically modified substrates have been reported to favor cell differentiation [37,38]. It has been postulated that size, diameter and spacing of nanostructures control the focal adhesion assembly [39,40], influence the formation of F-actin [41], change the structure of the cytoskeleton-related proteins [42,43], and finally influence the cell nuclei to modify gene expression as well as other cellular behaviors [44,45]. Along with the cell morphology alterations, cytoskeletal F-actin arrangement is another factor influencing cell function and differentiation. Temporary changes in actin cytoskeleton have been shown to increase ALP activity, osteocalcin secretion and mineralization of the extracellular matrix by MC3T3-E1 cells [46].

X-ray photoelectron spectroscopy (XPS) analysis [18], contact angle and surface roughness measurements revealed differences in chemical composition, wettability and topography between flat and nanochannelar surfaces. These surface characteristics may affect biological and chemical events occurring on biomaterial surfaces, such as protein adsorption from serum, or surface chemical modifications leading to the differences we observed between the cells in contact with the two analyzed substrates in the present study.

3.2.4. Osteoclast Differentiation

In addition to osteoblast differentiation, the effect of nanochannelar topography on osteoclastogenesis was evaluated. For this, RAW 264.7 macrophages were seeded and cultured on the tested substrates in the presence of RANKL. Osteoclastogenesis was verified by TRAP expression using immunofluorescence staining (Figure 7a). TRAP is an enzyme that is proposed to be directly related to

osteoclast resorption activity [47,48]. On the flat control substrates, TRAP staining was diffused within the cytoplasm showing a higher intensity both at cell periphery and center. In osteoclasts cultured on nanochannels, TRAP was also distributed within the cytoplasm. However, a clear difference between the two materials was observed. Large TRAP-positive multinucleated cells were present on the control substrate, while on the nanochannelar surface much smaller multinucleated cells have been observed. It is worth noting that on both samples smaller cells, likely macrophages, are stained for TRAP. However, the proportion of TRAP-positive mononuclear cells to multinucleated cells was much higher in case of the nanochannels, indicating an overall alteration of osteoclast activation. The formation of large multinuclear cells following pre-osteoclast fusion is critical for osteoclast-mediated bone resorption [49]. The osteoclast size is related to bone resorption capacity; therefore, nanochannelar topography may prevent the fusion of pre-osteoclasts from forming large, mature osteoclasts.

Furthermore, enumeration of multinuclear TRAP-positive cells showed lower numbers on nanochannels than on control sample, but this difference was not significant (Figure 7b).

In order to look for topographically induced changes in osteoclastogenesis TRAP activity analysis was also performed. As shown in Figure 7c, TRAP activity expressed by the cells grown on nanochannelar substrates was significantly lower (~48%) than that exhibited on the control sample.

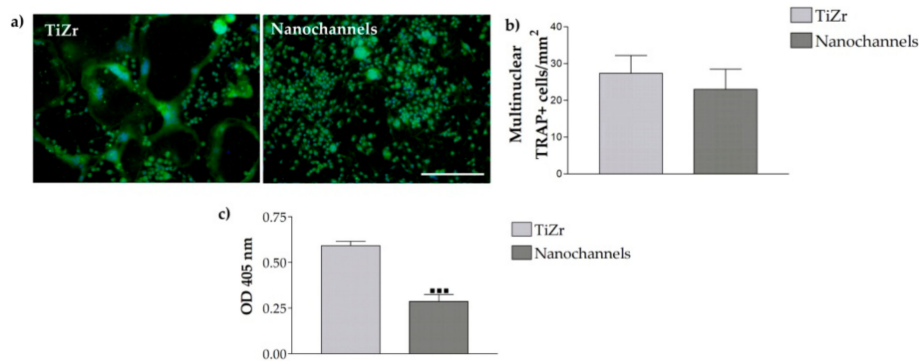


Figure 7. (a) Immunofluorescence staining of tartrate-resistant acid phosphatase (TRAP) (green fluorescence: TRAP signals, blue fluorescence: cell nuclei). RAW 264.7 cells were cultured for 7 days either on flat substrate or nanochannels with nuclear factor kappa-B ligand (RANKL) supplementation to the culture media. Scale bar represents 200 μm . (b) The average number of osteoclasts per mm^2 ; (c) Intracellular TRAP enzyme activity. Results are presented as means \pm SEM ($n = 3$); $p < 0.001$.

Further on, cells cultured and differentiated on the analyzed samples showed a modulation of the actin cytoskeleton organization. Microscopic examination revealed significant differences in the size of actin structures developed on the two topographies (Figure 8). On the flat TiZr surface, large podosome belts were predominant. On the nanochannelar surface, an opposite trend was observed: small podosome belts were the predominant phenotype, while large actin structures were missing. Although nanochannels caused shrinkage of differentiating osteoclasts, when compared to the control substrate, they showed no effect on the formation of the peripheral actin podosome belts.

It is worth mentioning that our findings are consistent with previous studies demonstrating that distinct topographies could differentially regulate osteoclast formation and activity. For example, fabrication of titania nanotubes by anodization on titanium surfaces has been shown to decrease the number of osteoclasts, TRAP activity, and the related gene expression compared to the pristine titanium [50]. Moreover, osteoclastogenesis inhibition was found to increase with increasing the nanotube diameter. Introduction of nanopillars on titanium substrates has also been shown to significantly reduce osteoclast differentiation and function [51]. However, several groups studying osteoclast formation and activation on metallic surfaces have reported different results. For instance, Sommer et al. assessed the impact of polished and sandblasted metallic surfaces on the osteoclastic differentiation of bone marrow cells co-cultured with osteoblasts under stimulation with

1,25(OH)₂D₃ [52], and reported that sandblasted surfaces enhanced osteoclast formation and function compared to the polished substrate, indicating that the rougher surfaces exhibit higher osteoclastogenic effects. In the case of Brinkmann et al., the effect of Ti substrates with smooth (TS), acid-etched (TA), and sandblasted acid-etched (TLA) surfaces on osteoclastogenesis was followed and compared with that on native bone (using RAW 264.7 cell lines) [53]. The results showed that the osteoclasts in contact with rough surfaces displayed similar cellular response in terms of cell size, actin ring formation and matrix metalloproteinase (MMP)-9 proteolytic activity as for native bone, whereas altered osteoclastogenesis was noticed on smooth titanium surface.

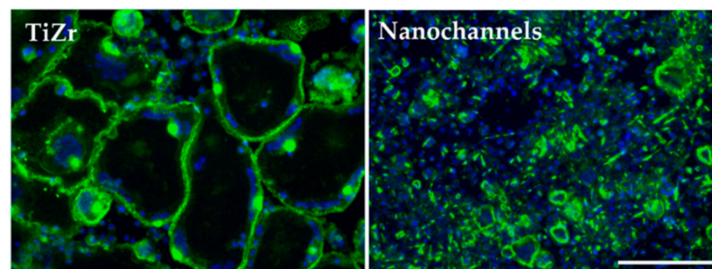


Figure 8. Immunofluorescence images of osteoclast formation on flat and nanochannelar surfaces after a 7-days stimulation with RANKL (green fluorescence: actin cytoskeleton, blue fluorescence: cell nuclei). Scale bar represents 200 μ m.

4. Conclusions

Our results indicate that the osteogenic abilities of the TiZr material were enhanced by the nanochannelar topography. Moreover, this specific topography was shown to inhibit the differentiation and maturation of osteoclasts derived from RAW 264.7 cells treated with RANKL. Therefore, this study provides a potential strategy to fabricate titanium-based implants able to inhibit bone resorption and improve osseointegration.

Author Contributions: Conceptualization, R.I., C.P., P.S. and A.C.; Formal analysis, R.I.; Funding acquisition, R.I. and C.P.; Investigation, R.I., A.M. and C.D.; Methodology, R.I., A.M., C.D. and A.C.; Project administration, R.I. and C.P.; Supervision, C.P., P.S. and A.C.; Validation, R.I., A.M., C.D., P.S. and A.C.; Writing-Original Draft, R.I., A.M. and C.D.; Writing-Review and Editing, C.P., P.S. and A.C.

Funding: This study was financially supported by the Romanian Ministry of National Education, CNCS-UEFISCDI, grant PED 97/2017.

Conflicts of Interest: The authors declare no conflicts of interest.

References

1. Karazisis, D.; Ballo, A.M.; Petronis, S.; Agheli, H.; Emanuelsson, L.; Thomsen, P.; Omar, O. The role of well-defined nanotopography of titanium implants on osseointegration: Cellular and molecular events in vivo. *Int. J. Nanomed.* **2016**, *11*, 1367–1382.
2. Kulkarni, M.; Mazare, A.; Park, J.; Gongadze, E.; Killian, M.S.; Kralj, S.; von der Mark, K.; Igljic, A.; Schmuki, P. Protein interactions with layers of TiO₂ nanotube and nanopore arrays: Morphology and surface charge influence. *Acta Biomater.* **2016**, *45*, 357–366. [[CrossRef](#)] [[PubMed](#)]
3. Zhang, Y.; Luo, R.; Tan, J.; Wang, J.; Lu, X.; Qu, S.; Weng, J.; Feng, B. Osteoblast behaviors on titania nanotube and mesopore layers. *Regen. Biomater.* **2017**, *4*, 81–87. [[CrossRef](#)]
4. Lv, L.; Liu, Y.; Zhang, P.; Zhang, X.; Liu, J.; Chen, T.; Su, P.; Li, H.; Zhou, Y. The nanoscale geometry of TiO₂ nanotubes influences the osteogenic differentiation of human adipose-derived stem cells by modulating h3k4 trimethylation. *Biomaterials* **2014**, *39*, 193–205. [[CrossRef](#)] [[PubMed](#)]
5. Son, W.W.; Zhu, X.; Shin, H.I.; Ong, J.L.; Kim, K.H. In vivo histological response to anodized and anodized/hydrothermally treated titanium implants. *J. Biomed. Mater. Res. Part B Appl. Biomater.* **2003**, *66*, 520–525. [[CrossRef](#)] [[PubMed](#)]

6. Park, J.; Bauer, S.; Schlegel, K.A.; Neukam, F.W.; von der Mark, K.; Schmuki, P. TiO₂ nanotube surfaces: 15 nm—An optimal length scale of surface topography for cell adhesion and differentiation. *Small* **2009**, *5*, 666–671. [[CrossRef](#)] [[PubMed](#)]
7. Park, J.; Bauer, S.; von der Mark, K.; Schmuki, P. Nanosize and vitality: TiO₂ nanotube diameter directs cell fate. *Nano Lett.* **2007**, *7*, 1686–1691. [[CrossRef](#)] [[PubMed](#)]
8. Su, E.P.; Justin, D.F.; Pratt, C.R.; Sarin, V.K.; Nguyen, V.S.; Oh, S.; Jin, S. Effects of titanium nanotubes on the osseointegration, cell differentiation, mineralisation and antibacterial properties of orthopaedic implant surfaces. *Bone Jt. J.* **2018**, *100*, 9–16. [[CrossRef](#)] [[PubMed](#)]
9. Chamberlain, L.M.; Brammer, K.S.; Johnston, G.W.; Chien, S.; Jin, S. Macrophage inflammatory response to TiO₂ nanotube surfaces. *J. Biomater. Nanotechnol.* **2011**, *2*, 293–300. [[CrossRef](#)]
10. Ma, Q.L.; Zhao, L.Z.; Liu, R.R.; Jin, B.Q.; Song, W.; Wang, Y.; Zhang, Y.S.; Chen, L.H.; Zhang, Y.M. Improved implant osseointegration of a nanostructured titanium surface via mediation of macrophage polarization. *Biomaterials* **2014**, *35*, 9853–9867. [[CrossRef](#)] [[PubMed](#)]
11. Neacsu, P.; Mazare, A.; Cimpean, A.; Park, J.; Costache, M.; Schmuki, P.; Demetrescu, I. Reduced inflammatory activity of RAW 264.7 macrophages on titania nanotube modified Ti surface. *Int. J. Biochem. Cell Biol.* **2014**, *55*, 187–195. [[CrossRef](#)] [[PubMed](#)]
12. Yao, S.; Feng, X.; Li, W.; Wang, L.-N.; Wang, X. Regulation of RAW 264.7 macrophages behavior on anodic TiO₂ nanotubular arrays. *Front. Mater. Sci.* **2017**, *11*, 318–327. [[CrossRef](#)]
13. Ercan, B.; Taylor, E.; Alpaslan, E.; Webster, T.J. Diameter of titanium nanotubes influences anti-bacterial efficacy. *Nanotechnology* **2011**, *22*, 295102. [[CrossRef](#)] [[PubMed](#)]
14. Ozkan, S.; Nguyen, N.T.; Mazare, A.; Hahn, R.; Cerri, I.; Schmuki, P. Fast growth of TiO₂ nanotube arrays with controlled tube spacing based on a self-ordering process at two different scales. *Electrochem. Commun.* **2017**, *77*, 98–102. [[CrossRef](#)]
15. Lu, H.; Fan, H.; Jin, R.; Chong, B.; Shen, X.; Yan, S.; Zhu, X. Formation and morphology evolution of anodic TiO₂ nanotubes under negative pressure. *Electrochim. Acta* **2016**, *215*, 380–387. [[CrossRef](#)]
16. Kapusta-Kolodziej, J.; Syrek, K.; Pawlik, A.; Jarosz, M.; Tynkevych, O.; Sulka, G.D. Effects of anodizing potential and temperature on the growth of anodic TiO₂ and its photoelectrochemical properties. *Appl. Surf. Sci.* **2017**, *396*, 1119–1129. [[CrossRef](#)]
17. Kowalski, D.; Kim, D.; Schmuki, P. TiO₂ nanotubes, nanochannels and mesosponge: Self-organized formation and applications. *Nano Today* **2013**, *8*, 235–264. [[CrossRef](#)]
18. Ion, R.; Stoian, A.B.; Dumitriu, C.; Grigorescu, S.; Mazare, A.; Cimpean, A.; Demetrescu, I.; Schmuki, P. Nanochannels formed on TiZr alloy improve biological response. *Acta Biomater.* **2015**, *24*, 370–377. [[CrossRef](#)] [[PubMed](#)]
19. Ion, R.; Vizireanu, S.; Stancu, C.E.; Luculescu, C.; Cimpean, A.; Dinescu, G. Surface plasma functionalization influences macrophage behavior on carbon nanowalls. *Mater. Sci. Eng. C* **2015**, *48*, 118–125. [[CrossRef](#)] [[PubMed](#)]
20. Ion, R.; Drob, S.I.; Ijaz, M.F.; Vasilescu, C.; Osiceanu, P.; Gordin, D.M.; Cimpean, A.; Gloriant, T. Surface characterization, corrosion resistance and in vitro biocompatibility of a new Ti-Hf-Mo-Sn alloy. *Materials* **2016**, *9*, 818. [[CrossRef](#)] [[PubMed](#)]
21. Neacsu, P.; Staras, A.I.; Voicu, S.I.; Ionascu, I.; Soare, T.; Uzun, S.; Cojocaru, V.D.; Pandele, A.M.; Croitoru, S.M.; Miculescu, F. Characterization and in vitro and in vivo assessment of a novel cellulose acetate-coated Mg-based alloy for orthopedic applications. *Materials* **2017**, *10*, 686. [[CrossRef](#)] [[PubMed](#)]
22. Mitran, V.; Dinca, V.; Ion, R.; Cojocaru, V.D.; Neacsu, P.; Dinu, C.Z.; Rusen, L.; Brajnicov, S.; Bonciu, A.; Dinescu, M.; et al. Graphene nanoplatelets-sericin surface-modified gum alloy for improved biological response. *RSC Adv.* **2018**, *8*, 18492–18501. [[CrossRef](#)]
23. Ion, R.; Gordin, D.M.; Mitran, V.; Osiceanu, P.; Dinescu, S.; Gloriant, T.; Cimpean, A. In vitro bio-functional performances of the novel superelastic beta-type Ti–23Nb–0.7Ta–2Zr–0.5N alloy. *Mater. Sci. Eng. C* **2014**, *35*, 411–419. [[CrossRef](#)] [[PubMed](#)]
24. Owen, T.A.; Aronow, M.; Shalhoub, V.; Barone, L.M.; Wilming, L.; Tassinari, M.S.; Kennedy, M.B.; Pockwinse, S.; Lian, J.B.; Stein, G.S. Progressive development of the rat osteoblast phenotype in vitro: Reciprocal relationships in expression of genes associated with osteoblast proliferation and differentiation during formation of the bone extracellular matrix. *J. Cell Physiol.* **1990**, *143*, 420–430. [[CrossRef](#)] [[PubMed](#)]

25. Biggs, M.J.; Richards, R.G.; Gadegaard, N.; McMurray, R.J.; Affrossman, S.; Wilkinson, C.D.; Oreffo, R.O.; Dalby, M.J. Interactions with nanoscale topography: Adhesion quantification and signal transduction in cells of osteogenic and multipotent lineage. *J. Biomed. Mater. Res. A* **2008**, *91*, 195–208. [[CrossRef](#)] [[PubMed](#)]
26. Biggs, M.J.P.; Dalby, M.J. Focal adhesions in osteoneogenesis. *Proc. Inst. Mech. Eng. H* **2010**, *224*, 1441–1453. [[CrossRef](#)] [[PubMed](#)]
27. Yim, E.K.F.; Darling, E.M.; Kulangara, K.; Guilak, F.; Leong, K.W. Nanotopography-induced changes in focal adhesions, cytoskeletal organization, and mechanical properties of human mesenchymal stem cells. *Biomaterials* **2010**, *31*, 1299–1306. [[CrossRef](#)] [[PubMed](#)]
28. Kim, D.-H.; Provenzano, P.P.; Smith, C.L.; Levchenko, A. Matrix nanotopography as a regulator of cell function. *J. Cell Biol.* **2012**, *197*, 351–360. [[CrossRef](#)] [[PubMed](#)]
29. Murphy, W.L.; McDevitt, T.C.; Engler, A.J. Materials as stem cell regulators. *Nat. Mater.* **2014**, *13*, 547–557. [[CrossRef](#)] [[PubMed](#)]
30. Abagnale, G.; Steger, M.; Nguyen, V.H.; Hersch, N.; Sechi, A.; Joussem, S.; Denecke, B.; Merkel, R.; Hoffmann, B.; Dreser, A.; et al. Surface topography enhances differentiation of mesenchymal stem cells towards osteogenic and adipogenic lineages. *Biomaterials* **2015**, *61*, 316–326. [[CrossRef](#)] [[PubMed](#)]
31. Lin, X.; Shi, Y.; Cao, Y.; Liu, W. Recent progress in stem cell differentiation directed by material and mechanical cues. *Biomed. Mater.* **2016**, *11*, 014109. [[CrossRef](#)] [[PubMed](#)]
32. Newman, P.; Galeano Niño, J.L.; Graney, P.; Razal, J.M.; Minett, A.I.; Ribas, J.; Ovalle-Robles, R.; Biro, M.; Zreiqat, H. Relationship between nanotopographical alignment and stem cell fate with live imaging and shape analysis. *Sci. Rep.* **2016**, *6*, 37909. [[CrossRef](#)] [[PubMed](#)]
33. Isaac, J.; Galtayries, A.; Kizuki, T.; Kokubo, T.; Berda, A.; Sautier, J.M. Bioengineered titanium surfaces affect the gene-expression and phenotypic response of osteoprogenitor cells derived from mouse calvarial bones. *Eur. Cells Mater.* **2010**, *20*, 178–196. [[CrossRef](#)]
34. Andrukhov, O.; Huber, R.; Shi, B.; Berner, S.; Rausch-Fan, X.; Moritz, A.; Spencer, N.D.; Schedle, A. Proliferation, behavior, and differentiation of osteoblasts on surfaces of different microroughness. *Dent. Mater.* **2016**, *32*, 1374–1384. [[CrossRef](#)] [[PubMed](#)]
35. Jäger, M.; Urselmann, F.; Witte, F.; Zanger, K.; Li, X.; Ayers, D.C.; Krauspe, R. Osteoblast differentiation onto different biometals with an endoprosthetic surface topography in vitro. *J. Biomed. Mater. Res. A* **2007**, *86*, 61–75.
36. Velasco-Ortega, E.; Alfonso-Rodríguez, C.A.; Monsalve-Guil, L.; España-López, A.; Jiménez-Guerra, A.; Garzón, I.; Alaminos, M.; Gil, F.J. Relevant aspects in the surface properties in titanium dental implants for the cellular viability. *Mater. Sci. Eng. C* **2016**, *64*, 1–10. [[CrossRef](#)] [[PubMed](#)]
37. Dalby, M.J.; Gadegaard, N.; Tare, R.; Andar, A.; Riehle, M.O.; Herzyk, P.; Wilkinson, C.D.; Oreffo, R.O. The control of human mesenchymal cell differentiation using nanoscale symmetry and disorder. *Nat. Mater.* **2007**, *6*, 997–1003. [[CrossRef](#)] [[PubMed](#)]
38. Oh, S.; Brammer, K.S.; Li, Y.S.J.; Teng, D.; Engler, A.J.; Chien, S.; Jin, S. Stem cell fate dictated solely by altered nanotube dimension. *Proc. Natl. Acad. Sci. USA* **2009**, *106*, 2130–2135. [[CrossRef](#)] [[PubMed](#)]
39. Lavenus, S.; Pilet, P.; Guicheux, J.; Weiss, P.; Louarn, G.; Layrolle, P. Behaviour of mesenchymal stem cells, fibroblasts and osteoblasts on smooth surfaces. *Acta Biomater.* **2011**, *7*, 1525–1534. [[CrossRef](#)] [[PubMed](#)]
40. Chen, C.S.; Alonso, J.L.; Ostuni, E.; Whitesides, G.M.; Ingber, D.E. Cell shape provides global control of focal adhesion assembly. *Biochem. Biophys. Res. Commun.* **2003**, *307*, 355–361. [[CrossRef](#)]
41. Pollard, T.D.; Cooper, J.A. Actin, a central player in cell shape and movement. *Science* **2009**, *326*, 1208–1212. [[CrossRef](#)] [[PubMed](#)]
42. Mendez, M.G.; Kojima, S.-I.; Goldman, R.D. Vimentin induces changes in cell shape, motility, and adhesion during the epithelial to mesenchymal transition. *FASEB J.* **2010**, *24*, 1838–1851. [[CrossRef](#)] [[PubMed](#)]
43. Damania, D.; Subramanian, H.; Tiwari, A.K.; Stypula, Y.; Kunte, D.; Pradhan, P.; Roy, H.K.; Backman, V. Role of cytoskeleton in controlling the disorder strength of cellular nanoscale architecture. *Biophys. J.* **2010**, *99*, 989–996. [[CrossRef](#)] [[PubMed](#)]
44. Rudolf, E.; Cervinka, M.; Cerman, J.; Schroterova, L. Hexavalent chromium disrupts the actin cytoskeleton and induces mitochondria-dependent apoptosis in human dermal fibroblasts. *Toxicol. In Vitro* **2005**, *19*, 713–723. [[CrossRef](#)] [[PubMed](#)]

45. Vetterkind, S.; Illenberger, S.; Kubicek, J.; Boosen, M.; Appel, S.; Naim, H.Y.; Scheidtmann, K.-H.; Preuss, U. Binding of par-4 to the actin cytoskeleton is essential for Par-4/Dlk-mediated apoptosis. *Exp. Cell Res.* **2005**, *305*, 392–408. [[CrossRef](#)] [[PubMed](#)]
46. Higuchi, C.; Nakamura, N.; Yoshikawa, H.; Itoh, K. Transient dynamic actin cytoskeletal change stimulates the osteoblastic differentiation. *J. Bone Miner. Metab.* **2009**, *27*, 158–167. [[CrossRef](#)] [[PubMed](#)]
47. Kirstein, B.; Chambers, T.J.; Fuller, K. Secretion of tartrate-resistant acid phosphatase by osteoclasts correlates with resorptive behavior. *J. Cell. Biochem.* **2006**, *98*, 1085–1094. [[CrossRef](#)] [[PubMed](#)]
48. Halleen, J.M.; Alatalo, S.L.; Suominen, H.; Cheng, S.; Janckila, A.J.; Vaananen, H.K. Tartrate-resistant acid phosphatase 5b: A novel serum marker of bone resorption. *J. Bone Miner. Res.* **2000**, *15*, 1337–1345. [[CrossRef](#)] [[PubMed](#)]
49. Takito, J.; Otsuka, H.; Yanagisawa, N.; Arai, H.; Shiga, M.; Inoue, M.; Nonaka, N.; Nakamura, M. Regulation of osteoclast multinucleation by the actin cytoskeleton signaling network. *J. Cell. Physiol.* **2014**, *230*, 395–405. [[CrossRef](#)] [[PubMed](#)]
50. Li, Y.; Li, F.; Zhang, C.; Gao, B.; Tan, P.; Mi, B.; Zhang, Y.; Cheng, H.; Liao, H.; Huo, K.; et al. The dimension of titania nanotubes influences implant success for osteoclastogenesis and osteogenesis patients. *J. Nanosci. Nanotechnol.* **2015**, *15*, 4136–4142. [[CrossRef](#)] [[PubMed](#)]
51. Silverwood, R.K.; Fairhurst, P.G.; Sjöström, T.; Welsh, F.; Sun, Y.; Li, G.; Yu, B.; Young, P.S.; Su, B.; Meek, R.D.M.; et al. Analysis of osteoclastogenesis/osteoblastogenesis on nanotopographical titania surfaces. *Adv. Healthc. Mater.* **2016**, *5*, 947–955. [[CrossRef](#)] [[PubMed](#)]
52. Sommer, B.; Felix, R.; Sprecher, C.; Leunig, M.; Ganz, R.; Hofstetter, W. Wear particles and surface topographies are modulators of osteoclastogenesis in vitro. *J. Biomed. Mater. Res. A* **2004**, *72*, 67–76.
53. Brinkmann, J.; Hefti, T.; Schlottig, F.; Spencer, N.D.; Hall, H. Response of osteoclasts to titanium surfaces with increasing surface roughness: An in vitro study. *Biointerphases* **2012**, *7*, 34. [[CrossRef](#)] [[PubMed](#)]



© 2018 by the authors. Licensee MDPI, Basel, Switzerland. This article is an open access article distributed under the terms and conditions of the Creative Commons Attribution (CC BY) license (<http://creativecommons.org/licenses/by/4.0/>).